Chapter 2. Type-I CdSe@ZnX (X=S, Se) Core/Shell Quantum Dots and their Applications

2.1. Introduction

Due to their remarkable size dependent photophysical properties and versatility toward chemical modification, semiconductor nanoparticles have received considerable attention.[1-10] Semiconductor nanoparticles such as cadmium chalcogenides with high luminescence yield, monodispersion, uniform size and shape have played an active role in biological labeling reagents.[11-18] Among numerous applications, the core/shell types of quantum dots have been proven to serve as a better probe than the bare core ones owing to their higher emission quantum efficiency (quantum confinement) and thermal stability (protective surface), in particular when subject to subsequent multiple-step chemical modification.[19-30]

The use of dimethyl cadmium $Cd(CH_3)_2$ as a precursor in the process for the synthesis of high-quality cadmium chalcogenides has been well documented.[31-35] Unfortunately, the high toxicity and pyrophoric liability limit its availability in many places. Alternatively, CdO has recently been reported to be an ideal precursor toward synthesizing core Cd chalcogenide nanocrystals.[27,35,36] Its lower toxicity and good thermal stability make the synthetic route to Cd chalcogenides quantum dots feasible without restrictions on equipment and on severe conditions. Very recently, based on the CdO precursor Reiss et al.[27] reported a new synthetic route for the core/shell CdSe@ZnSe nanoparticles incorporating preparation, separation and purification of core material (CdSe), followed by a second-step shell (ZnSe) deposition.

In the course of developing chemically modified nanoparticles, on the premise of safety and available resources, I have made attempts to prepare CdSe@ZnX

nanocrystals via the CdO precursor. Although the two-step approach is salient, a successful CdSe@ZnSe preparation from CdO in terms of good homogeneity in size distribution and luminescence efficiency greatly relies on the purity of core CdSe prior to the shell deposition.[27] Furthermore; the second-step core/shell synthesis involves a subtle mixing procedure between core and reagents for the shell, which inevitably requires extensive work. These concerns have motivated our and Professor Chou's laboratories, as a collaboration project, to seek an alternative modification, aiming at simplicity in methodology with high particle quality being preserved. On the basis of one-pot reaction, in this chapter, I will first describe a simple, reproducible synthetic protocol for preparing high-quality CdSe@ZnX core/shell nanoparticles.

From the applications viewpoint, I have further made attempts to chemically modify QDs so as to develop specific molecular probes, of which the metal ion sensing is of prime importance. Sensing toxic metal ions is essential in monitoring of the environment, the control of chemical processes, and medical applications. Of particular importance is the selective detection of the mercury ion (II), which is biologically highly toxic and is known to cause a variety of phenomena in humans, such as damage to the central nervous system and resulting neuropsychiatric disorders. Currently existing sensors for the detection of Hg^{2+}, such as thin-films device of gold,[37] organic probes,[38,39] polymeric materials[40] and bio-composites,[41] are subject to certain inferiorities. These include high operation temperatures and complexity,[37] relatively low sensitivity, non-aqueous environments,[39,42] and slow response due to the long-time equilibrium.[41] Very recently, Palomares et al.[43] demonstrated an exquisite system for the colorimetric sensing of mercury ion (II) in aqueous solution, in which the sensing mechanism incorporates a transformation of the thiocyanate ligands of the probing Ru(III) complex induced by Hg^{2+} ions, resulting in a change of

the Ru(III) energy gap and hence the color.[43] To further extend the detection limit, a mercury ion (II) sensing design exploiting the fluorescence property warrants our attention. In this thesis, based on the syntheses of highly emissive, water-soluble CdSe@ZnS (core/shell) quantum dots (QDs) capped by dihydrolipoic acid (DHLA), I like to present a highly sensitive/selective fluorogenic sensor to probe the mercury ion (II) in both aqueous solution and heterogeneous solid film.

From yet another approach, ionophores are usually coupled with a molecular chromophore, of which the associated spectral properties in either absorption or emission are sensitive to the environmental stimuli. Up to this stage, a large portion of chromophores being developed are hydrophobic, which consequently limits their applications in aqueous media. Recently, metal nanoparticles have been emerged as an important colorimetric reporter due to their extremely high extinction coefficient (i.e. absorptivity) that is also very sensitive to the transition from mono-dispersion to the aggregation, resulting in a distinct color change.[44-50] For the case of gold nanoparticles, this phenomenon of which is well known as the surface plasmon absorption, the color change upon aggregation is due to the coupling of the surface plasmon resonance as a result of the proximity between two Au nanoparticles.[52,53] Recently, based on a sandwich complex of 2:1 between 15-crown-5 and K^+, Chen and coworkers[53] reported on capping the Au nanoparticles with the 15-crown-5 functionality and the resulting 15-crown-5 functionalized Au nanoparticles were successfully exploited as a novel prototype to probe K^+, in which the transduction is signified by subtle changes of the surface plasma resonance, i.e. a colormetry type of sensing mechanism. On this basis, other crown ether-modified metal nanoparticles, especially those of II-VI and III-V semiconductor composites, may serve as an alternative, taking advantages of their superior fluorescence properties such as high quantum efficiency and narrow

bandwidth (good contrast luminescence color), etc. In this chapter, I also like to elaborate the work on the design and synthesis of 15-crown-5 functionalized, water soluble CdSe@ZnS quantum dots (QDs) as well as their exploitation as a sensing unit toward K^+ in aqueous solution. The sensing mechanism utilizing either aggregation property in single size QDs as well as the Förster type of energy transfer in dual color QDs system renders a great versatility and flexibility in view of future applications.

2.2. Experimental Section

2.2.1. Chemicals

Tri-*n*-octylphosphine oxide (TOPO, tech. grade 90 %), tri-*n*-butylphosphine (TBP, tech. grade 98 %) and hexadecylamine (HDA, 90 %) were purchased from Aldrich, SHOWA and TCI, respectively. In another approach, high purity TOPO (99%, Aldrich) was also applied for a comparative study. CdO (99.99%), selenium (Se) powder 200 mesh (> 99.5 %) and sulfur (S) powder (99.5 %) were obtained from Strem, ACROS and Alfa Aesar, respectively. Zinc stearate (Riedel-deHaën) was purchased from Riedel-deHaën and used immediately after receipt. Dimethylzinc ($Zn(CH_3)_2$, 2M solution in toluene) and hexamethyldisilathiane ($(TMS)_2S$) were acquired from Aldrich. All reagents were used as received.

2.2.2. Method 1 – for Size Tuning

Due to great concerns in the tunability of nanocrystals, a size tunable one-pot CdSe@ZnX synthesis was described at first. Here, a mixture of CdO (0.04 g), HDA (5.67 g) and TOPO (5.67 g) was heated up to 340 ^oC under Ar flow on a Schlenk line. After the formation of a CdO-HDA complex, as indicated by the solution turning from color reddish to colorless, the system was allowed to cool to 260 ^oC. As the

temperature stabilized at 260 ^{o}C for around 3-5 hr, Se@TBP (0.03 g in 6 ml TBP) was quickly injected (< 2 sec) into the hot CdO@HDA/TOPO solution to proceed with the nucleation and the growth of CdSe nanocrystals. Due to the introduction of large amounts of TBP, the system temperature was further decreased to 230 ^{o}C within 30 sec. Subsequently, the ZnX@TBP shell stock solution was injected precisely to the core solution via the syringe pump at a rate 0.1-0.15 ml/min, while the temperature remained at 230 ^{o}C. The growth of CdSe@ZnX quantum dots then could be extracted. The injection of shell stock solution was divided into five portions in 20 sec intervals to minimize the nucleation of shell particles.[19] Upon injecting all the ZnX@TBP shell stock solution, the reaction-mixture was allowed to cool and stir at 110 ^{o}C for a period of 1-2 hr. The final molar ratio between Cd/Se (core) and Zn/X (shell) was kept constant, typically ~1:4.

ZnX@TBP shell stock solution was prepared form two types of precursors. For the first approach, a pyrophoric precursor was used by dissolving dimethylzinc (~125 μl) and hexamethyldisilathiane (~130 μl) in TBP (5.3 ml) at room temperature. In other approach, zinc stearate was used as a shell precursor to achieve safety and green chemistry, which has been proven to be appropriate for the growth of ZnSe shells upon the CdSe nanocrystals,[27] even if there is a large lattice mismatch between CdSe and ZnSe.[28,29] In this study, zinc stearate (0.76 g) and sulfur powder (0.02 g) in TBP (5.3 ml) were used and heated to 110 ^{o}C around 30 min. The stock solution of shell was prepared then cooled to room temperature for the subsequent core/shell synthesis.

In the core/shell formation above, the precursor concentrations were diluted largely by TBP and HDA, resulting in a significant reduction of the particle growth rate. The resulting nanocrystals with selective diameters/thickness could be extracted at different aging times. Consequently, the tunability of CdSe@ZnS nanocrystals was

largely elevated.

2.2.3. Method 2 – for Size Uniform

It was not only attempted to produce on large scale by the one-pot CdSe@ZnS, but aimed at unique-size distribution. In order to achieve this goal, method 1 (section 2.2.2.) was modified by optimizing the reaction parameters such as Cd/Se ratio, TBP/HDA concentrations, etc. (vide infra). For a typical approaching, CdO (0.04 g), TOPO (5.67 g) and HDA (2.83 g) were first loaded in a 50 ml three-neck flask and heated to 340 ^{o}C under argon flow on a Schlenk line. After forming a CdO-HDA complex, the system was then cooled down to 260 ^{o}C, followed by a rapid (< 2 sec) injection of the Se@TBP stock solution (0.013 g Se in 1 ml TBP). After this process the temperature was cooled down to 230 ^{o}C within a long period of 20 min, then passivated the ZnX shell by the addition of ZnX@TBP. The ZnX@TBP shell stock solution was similarly prepared from the aforementioned methods. The injection of shell stock solution was also divided into five portions in 20 sec intervals at a rate 0.05-0.15 ml/min to avoid small size particles and/or alloy formation. Upon injecting all the ZnX@TBP shell stock solution, the reaction-mixture was then incubated at 110 ^{o}C for a period of 1-2 hr to obtain CdSe@ZnX particles with an emission maximized typically at 635 nm.

For the above-described methods, purification was performed by adding anhydrous methanol to precipitate the resulted nanocrystals, which were then accumulated by centrifuging. This precipitation/centrifugation process was repeated several times to further remove unreacted residues. A slight decrease in the quantum efficiency was observed during the purification process, and could be regained by adding an adequate amount of TBP in each interval of centrifugation.[54] The resulting nanocrystals were redispersed in anhydrous toluene for further characterization.

Further attempt is tuning the growth rate of CdSe@ZnS nanocrystals were made by varying temperatures from [260 ^{o}C (Se@TBP); 230 ^{o}C (shell)] to [230 ^{o}C; 180 ^{o}C]. The lower nucleation/growth temperature leads to the large reduction of the growth rate, so that particles with emission maxima between 560 and 600 nm could be obtained during a long separated period of 1 hr. The vastly extended aging time at lower temperatures provides great potential in synthesizing wide-tunable-range core/shell nanoparticles for future applications in multiple bio-labeling or LEDs. Unfortunately, the resulting nanocrystals revealed a small fraction of dual emission, possibly due to the alloy formation (vide infra).

2.2.4. Synthesis and Water-Soluble CdSe@ZnS QDs

2.2.4.1 DHLA Capping

Although we described the synthetic method 1 of one-pot synthesis core/shell type QDs was more conveniently and highly reproducible in our research (vide infra). However, it is lack of purification for the CdSe core step result in QY of the final product (i.e. CdSe@ZnS QDs) was not maintain as high as well condition. For the high quality and surface perfect CdSe@ZnS QD used in water-soluble modification, we decide to prepare the CdSe@ZnS QDs by two-step method. The water-soluble CdSe@ZnS nanoparticles were prepared using a stepwise procedure reported by Mattoussi et al.[55] with a slight modification. Briefly, TBP/TOPO-capped CdSe@ZnS core/shell particles were prepared from the growth and annealing of CdO.[27] TBP/TOPO capping groups were subsequently exchanged with 20 mg DHLA (freshly prepared from distilled thioctic acid by sodium borohydride reduction)[56] placed in a reaction vessel. 15 mL of methanol was added and the pH value was adjusted to 10~11 with tetramethylammonium hydroxide pentahydrate. Under dark conditions, 10 mg of CdSe@ZnS nanocrystals were dissolved in the mixture, and the vessel was

placed under regular airflow. The mixture was heated under reflux at 65 °C overnight, and then the reaction was terminated and the mixture allowed to cooling to room temperature overnight. The DHLA-capped nanocrystals were then precipitated with diethyl ether. For further purification, methanol was added to dissolve the precipitate, followed by the addition of diethyl ether to reprecipitate the nanocrystals.which absorption and emission spectra were shown in Figure 2.1.

2.2.4.2 Crown-Dithiolcapping

Preparation of mercaptoalkanoic crown ether (MCE): Scheme 2.1 depicts the synthetic route of MCE, in which 2-(hydroxymethyl)-15-crown 5-ether and thioctic acid were added to CH_2Cl_2. The mixture was stirred for 15 min at 0 °C under N_2. Then dicyclohexyl carbodiimide (DCC) and 4-dimethylaminopyridine (DMAP) in cold CH_2Cl_2 were added to the above solution, and the mixture was stirred for another 15 min at 0 °C. The cooling bath was then removed, and the solution allowed to heat up to room temperature. After stirring for 72 h under N_2, the reaction mixture was filtered through a fine glass frit to yield a clear, pale yellow filtrate and insoluble urea byproduct as a fine, white gray powder. The clear filtrate was washed with water, acetic acid aqueous solution, and finally again with water.

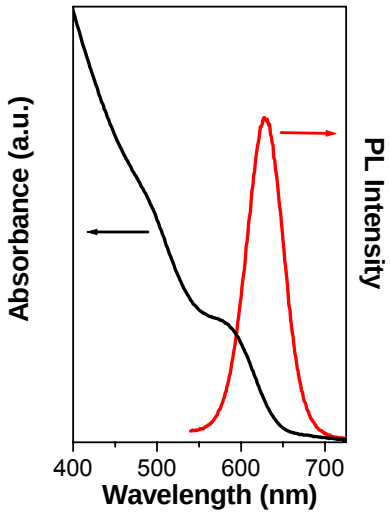

Figure 2.1 The absorption and emission spectra of DHLA capped CdSe@ZnS (core, 4.1 nm, shell, 1.2 nm) in H_2O (pH = 7~8).

The organic later was subjected to column chromatography on silica gel. ^{1}H NMR ($CDCl_3$, 400 MHz) δ 1.40-1.52 (m, 2H), 1.61-1.73 (m, 4H), 1.84-1.93 (m, 1H), 2.33 (t, *J* =7.2 Hz, 2H), 2.40-2.48 (m, 1H), 3.06-3.19 (m, 2H), 3.51-3.57 (m, 2H), 3.58-3.76 (m, 16H), 3.78-3.84 (m, 2H), 4.04-4.09 (m, 1H), 4.19-4.23 (m, 1H); ^{13}C

NMR ($CDCl_3$, 100 MHz) δ 24.8, 28.9, 34.1, 34.7, 38.6, 40.3, 56.4, 64.2, 70.3, 70.4, 70.5, 70.6, 70.8, 70.9, 71.0, 71.1, 173; HRMS Cacld. for $C_{19}H_{34}O_7S_2$: 438.1746 found:438.1744

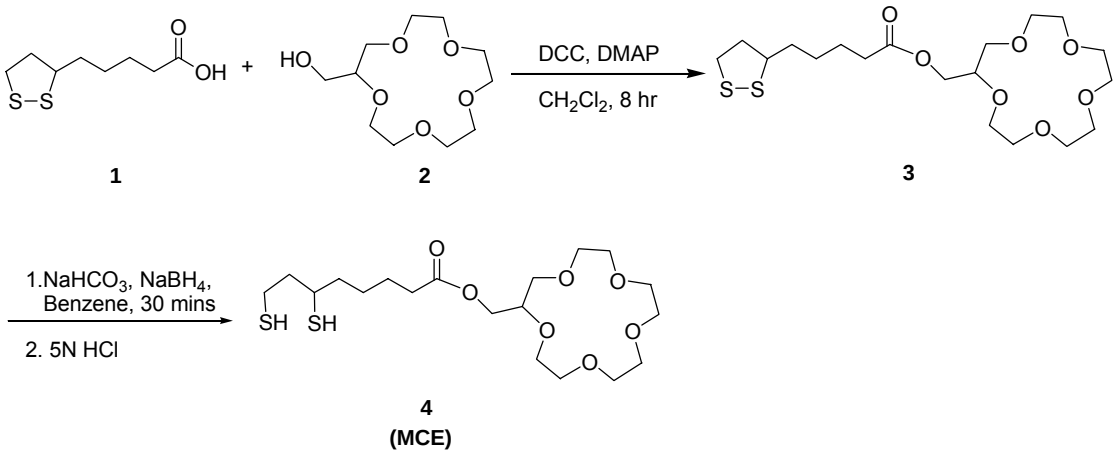

Scheme 2.1 The synthetic route of preparing MCE.

Modification of CdSe@ZnS QDs with MCE: The water-soluble CdSe@ZnS QDs were prepared using a stepwise procedure reported by Mattoussi et al.[55] with a slight modification. Briefly, TBP/TOPO-capped CdSe@ZnS core/shell particles were prepared from the growth and annealing of CdO.[27] TBP/TOPO capping groups were subsequently exchanged with 40 mg MCE placed in a reaction vessel. 15 mL of methanol was added and the pH was adjusted to > 10 with tetramethylammonium hydroxide pentahydrate. Under dark conditions, 10 mg of CdSe@ZnS nanocrystals were dissolved in the mixture, and the vessel was placed under regular airflow. The mixture was heated under reflux at 65 ^{o}C overnight, and then the reaction was terminated and the mixture allowed to cooling to room temperature overnight. The MCE-capped CdSe@ZnS nanocrystals were then precipitated with ethyl acetate. For further purification, methanol was added to dissolve the precipitate, followed by the addition of ethyl acetate to reprecipitate the nanocrystals.

2.2.5. Measurement

The shapes of QDs were obtained with a Hitachi H-7100 transmission electron microscope (TEM). UV-Vis steady-state absorption and emission spectra were recorded by a Hitachi (U-3310) spectrophotometer and an Edinburgh (FS920) fluorimeter, respectively. Both wavelength-dependent excitation and emission response of the fluorimeter have been calibrated. DCM (4-(Dicyanomethylene)-2-methyl-6-(*p*-dimethylaminostyryl)-4*H*-pyran, λ_{em} = 615 nm, Exciton) in methanol with Φ of ~ 0.43[57] served as the standard for measuring the emission quantum yield. Nanosecond lifetime studies were performed by an Edinburgh FL 900 photon-counting system with a hydrogen-filled/or a nitrogen lamp as the excitation source. Data were analyzed using the nonlinear least squares procedure in combination with an iterative convolution method. The emission decays were analyzed by the sum of exponential functions, which allows partial removal of the instrument time broadening and consequently renders a temporal resolution of ~200 ps. Solvents such as toluene were of spectragrade quality (Merck Inc.) and used right after received.

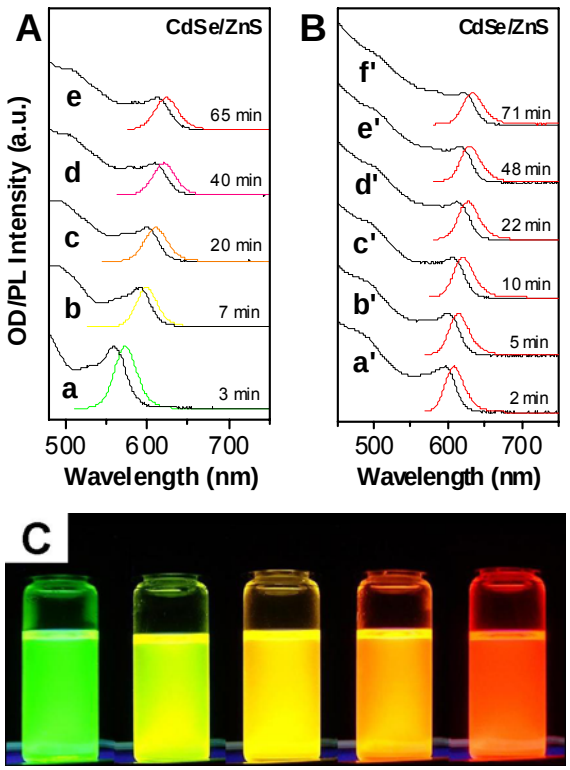

Figure 2.2 Absorption and emission spectra of CdSe@ZnS in toluene prepared from (A) method 1 and (B) method 2 (see text for the detailed description). The time scale for (A) and (B) is counted from the addition of Se@TBP (C) Authentic emission color of different shell thickness CdSe@ZnS nanocrystals acquired by a hand-held UV lamp with 366 nm excitation.

2.3. Results and Discussion

2.3.1. Reaction Parameters

Figure 2.2A depicts the absorption and emission spectra of

various sizes of CdSe@ZnS quantum dots prepared according to the tunable wavelength, one-pot reaction scheme (i.e. method 1). In each prepared sample the size distribution is rather small, as indicated by their narrow emission fwhm of 30 nm as well as uniformity in the excited-state relaxation dynamics (τ_f ~20-25 ns, see Table 2.1). Direct evidence of size distribution was given by the results of the TEM (transmission electron microscopy) image. For instance, the TEM image of the batch extracted at τ_f ~600 nm revealed a fairly homogeneous size distribution of 5.5 ±0.6nm (see Figure 2.4). High luminescence efficiency was observed in all the different sizes of quantum dots with quantum yields measured to be in the range of 0.4-0.7 (see Table 2.1). As shown in Figure 2.1B, based on method 2, the nearly time-independent, unique size CdSe@ZnS nanocrystals were obtained throughout the reaction with a systematic emission maximized at 635 nm. Using pyrophoric precursors, the quantum efficiency of the resulting CdSe@ZnS nanocrystals would consistently exceed 0.5, while it was slightly lower (0.3-0.5) by using the zinc stearate precursor, possibly due to its lower reactivity during the one-pot reaction.

Table 2.1 Photophysics of various batches of quantum dots synthesized from this study

	Method 1 (tunable size)				**Method 2 (unique size)**		
C@S type[a]	CdSe@ZnS^p				CdSe@ZnS^p	CdSe@ZnSe^z	CdSe@ZnS^z
Compound[b]	a	b	c	d	f'	f_1	f_2
PL (λ_{max})	560	574	598	622	635	630	632
PL QY (%)[c]	46.2	51.3	67.3	65.1	52.8	48.5	49.7
τ_f (ns)	18.1(80[d])	20.3(85)	23.1(81)	21.2(91)	17.2(88)	20.1(80)	19.9(86)

[a] Superscript *p*, *z* denotes pyrophoric, zinc stearate related precursors respectively. [b] Compounds listed here correspond to Fig. 2.3; f_1, f_2. not shown in Fig.31 correspond to the last batch (~70min) of CdSe@ZnSe^z, CdSe@ZnS^z nanocrystals, respectively. [c] Reference for the quantum yield measurement is Rhodamine 6G. [d] % of the major decay component.

The initial Cd/Se molar ratio and precursor concentrations turn out to be key factors for obtaining size variable core/shell versus fixed-size nanocrystals within one-pot reaction. In this study, under optimized experimental conditions the initial Cd/Se ratio varied from 0.7 (in method 1) to 2.0 (in method 2), indicating the shift of

the reaction parameters from a Se-rich to Cd-rich condition. Because the one-pot reaction scheme incorporates simultaneous growth of core and shell, the possibility of alloy formation has been carefully examined. Largely increasing the Cd/Se ratio caused adverse effects in method 1. For example, if we applied a Cd/Se ratio of > 2.0, a minor, broad emission peak centered at 500 nm was observed, indicating a possible formation of $Cd_xZn_{1-x}S$ alloy (vide infra). In this study, it was found that the alloy formation could be avoided by reducing the Cd/Se ratio to < 0.7 in method 1.

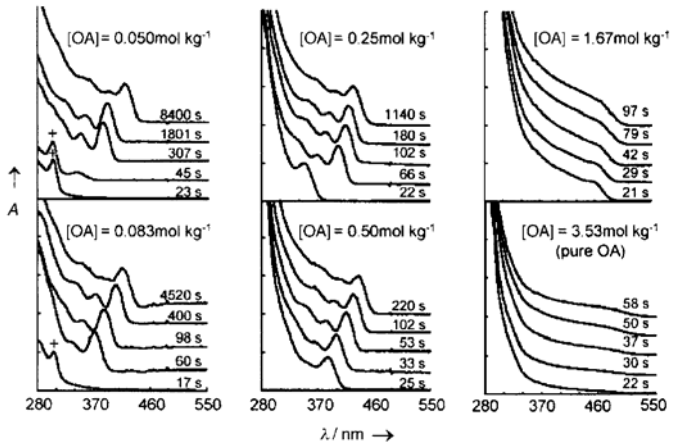

Figure 2.3 Temporal evolution of the absorption spectrum of the CdS QDs grown in ODE and different OA concentration.[58]

condition is suitable in method

On the other hand, due to the extended aging time for core growth prior to the shell addition in method 2, the possibility of alloy formation is considered small. Moreover, the higher Cd/Se ratio has been proven to have advantage in focusing the size distribution for hours before defocusing occurs.[33] Consequently, the Cd-rich 2. Detailed characterizations of the core/shell formation are elaborated in section **2.3.2.**

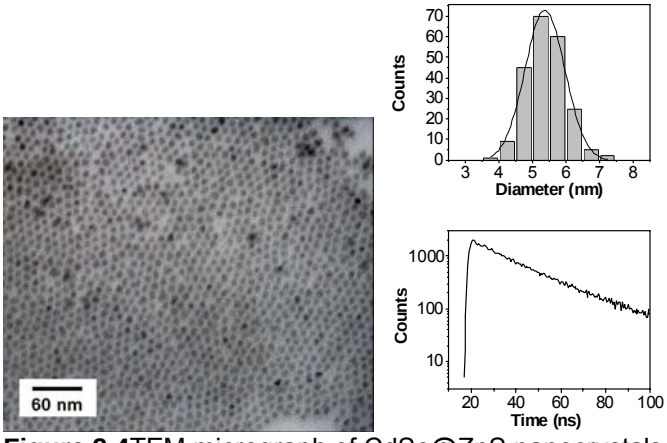

Figure 2.4TEM micrograph of CdSe@ZnS nanocrystals prepared by the tunable-size method (left), size distribution (upper right) and relaxation dynamics of compound **c** depicted in Figure 2.1.

The large increase of surfactants in method 1 dilutes precursor concentrations and consequently slows down the growth rate of core particles, so that the reaction time span is sufficiently long enough to deposit shell reagents at various core sizes. On one hand, as the precursor concentration is decreased, a large distribution of particle size is expected according to the Ostwald-Ripening defocusing mechanim,[33,59] which explains that as the precursor concentrations decrease, the critical size of particles increases. As a result, the growth of smaller particles during the reaction may serve as nutrients for the larger ones, resulting in an increase in particle size as well as size distribution. On the other hand, it has been well documented that an increase of HDA leads to a reduction of size distribution, of which the phenomenon is analogous to a refocusing process.[27,30,60] The interplay between these two opposite effects can be compensated for by optimizing HDA/TBP concentrations, giving rise to decent particle-size tunablity with small size distribution as described in this study. In comparison, the time-independent, unique size distribution obtained in method 2 can be qualitatively rationalized by the use of sufficiently low surfactant concentrations. Since surfactants act as capping agents as well as solvents, the precursor concentrations increase accordingly and the growth rate of the core is largely accelerated, eventually reaching a saturation of the particle size in a very short period. This synthetic protocol is particularly useful when a quick, large-scale synthesis of CdSe@ZnS nanocrystals is required without special consideration of the emission peak frequency.

One reaction parameter deserves to be further discussed is the technical grade TOPO of 90% purity applied in our synthetic scheme. One might consider the impurity existing in TOPO, which mainly consists of octylphosphonic acid, may interfere with the CdO complex formation. To examine such a possibility, we

performed control experiments by comparing HDA/TBP and TOPO (tech.-grade)/TBP solvent systems in synthesizing CdSe nanoparticles. In the HDA/TBP system a color evolution from reddish to colorless was observed during the elevation of temperature. In contrast, for the CdO-TOPO mixture the reddish color remained unchanged for more than 4 hr at 340 ^{o}C. The results clearly indicate that the complex formation for CdO is mainly assisted by HDA. Further support was given by the synthesis of CdSe nanoparticles using high-purity TOPO (99%) in the HDA/TOPO system. Under the same one-pot reaction condition, we obtained the corresponding nanoparticles with optical properties similar to that synthesized by the tech.-grade TOPO.

2.3.2. Products Characterization

Various techniques/spectroscopy were exploited to characterize the prepared nanocrystals. As shown in Figure 2.5a,b, the elemental analysis based on the energy dispersive spectroscopy (EDX) offered an unambiguous evidence for the presence of Cd/Se, Zn/S (or Zn/Se) components. Furthermore, X-ray photoelectron spectroscopy

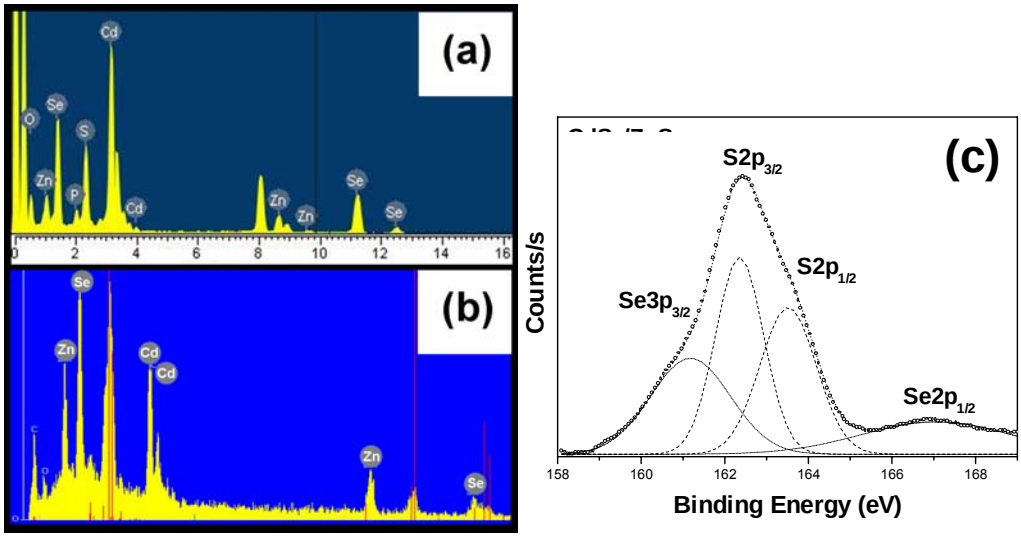

Figure 2.5 Energy dispersive spectroscopy (EDX) characterization of **a**) CdSe@ZnS and **b**) CdSe@ZnSe nanocrystals prepared by the one pot reaction described in the text. **c)** X-ray photoelectron spectroscopy (XPS) characterization of CdSe@ZnS core/shell nanoparticles. The experimental data of CdSe@ZnS is fitted by four Gaussians peaks representing a S2p (dashed) and Se3p (dotted) contribution.

(XPS) signals collected on core/shell CdSe@ZnS nanocrystals also clearly indicated the co-existence of S and Se in the core/shell structure by the appearance of the characteristic peaks such as $S2p_{1/2}$, $S2p_{3/2}$, $Se3p_{1/2}$, and $Se3p_{3/2}$ (see Figure 2.5c). We have also performed X-ray powder diffraction to examine the patterns of a series of CdSe and CdSe@ZnS nanoparticles. As shown in Figure 1.8, upon ZnS encapsulation the diffraction patterns shift gradually to high reflection angles. The result is a similar trend as that reported by Dabbousi et al.[24] on the growth of core/shell nanoparticles. Note recent studies on ternary $Cd_xZn_{1-x}S$ nanocrystals also indicated that by decreasing the Cd/Zn molar ratio in alloy the diffraction patterns gradually, 2θ shifted to higher values. However, for a homogeneous alloy one would expect a narrowing XRD peak width upon increasing the particle size.[61] In contrast, a slightly peak broadening was observed upon the shell addition (see Figure 2.6), supporting the core/shell formation in the one-pot reaction scheme. More characterization of the core/shell composition is elaborated as follows.

For nanocrystals with alloy compositions one would expect a blue shift of the first exciton peak upon increasing the dopant concentration.[61] Furthermore, for the $Cd_xZn_{1-x}S$ alloy a characteristic broad emission band at the region of 480-550 nm is normally expected.[62,63] In our tunable-size reaction scheme, the systematic red shift of the absorption/emission spectra upon the encapsulation of ZnS (or ZnSe), in combination with the absence of < 550 nm emission, negates the possibility of alloy formation. Nevertheless, as was mentioned in the previous section, when the initial Cd/Se ratio in method 1 was increased to as high as > 2.0, dual emission appeared, in which the minor one maximized at 500 nm may partially be attributed to the formation of $Cd_xZn_{1-x}S$ composites.

Theoretically, comparing the core only with the same diameter, spectral red shifts in core/shell nanoparticles are mainly due to the extent of excited electron wavefunction into the shell region, of which the degree of shifting depends on the band-offset between core and shell. However, with a large band-offset, the probability of excited electrons populated at the shell region is considered small. Accordingly, due to their large band-offset a small spectral red shift is predicted upon CdSe@ZnX formation, which apparently cannot rationalize the 60 nm tunability throughout the one-pot reaction. The results clearly indicate that HDA/TBP simultaneously controlled the growth of core particles and the shell encapsulation. The combination of these two factors plays a key role in fine-tuning the wavelength (i.e., size) and/or shell thickness.

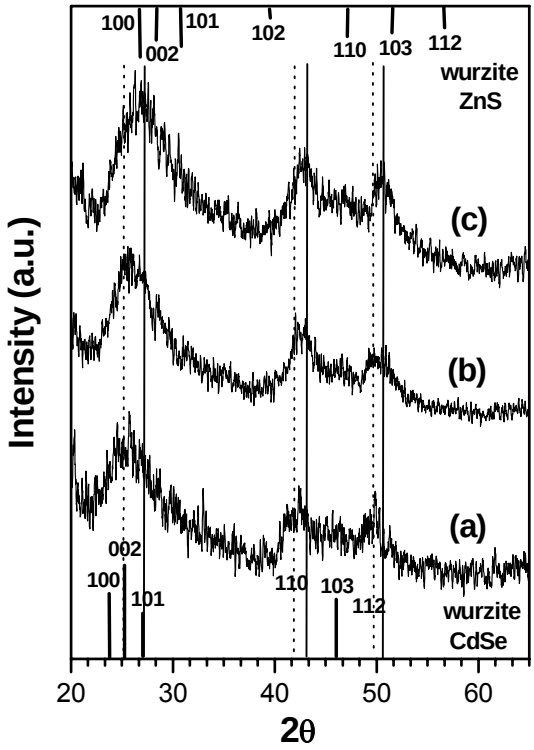

Figure 2.6 Series X-ray powder diffraction patterns of (a) core CdSe nanocrystals with diameter 4.6 nm, (b) core/shell CdSe@ZnS overcoated with 1.5 ZnS monolayer and (c) ~3.6 monolayer ZnS overcoated CdSe@ZnS nanoparticles. The solid vertical lines represent peak positions for sample (c, Fig. 2.7); the dotted lines represent pure wurzite CdSe crystal patterns. An evolution of peak shifting to higher 2 value is detected upon shell passivation. The patterns for wurzite ZnS and CdSe are shown for comparison at the top and bottom insets, respectively.

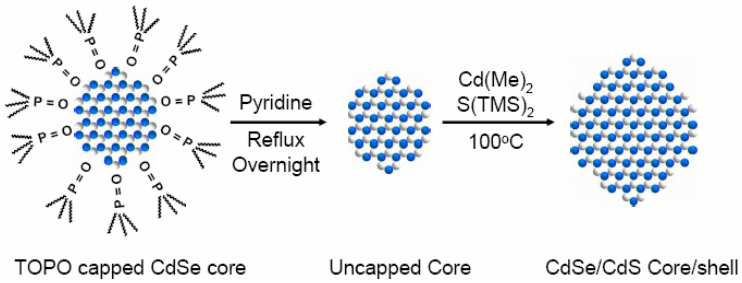

Figure 2.7 Synthesis of CdSe/CdS QDs by pyridine coated on the CdSe core.

Finally, control experiments have been performed based on the tunable-size synthetic protocol to compare the properties between core only and core/shell nanoparticles. Under identical experimental conditions, i.e., the same Cd/Se ratio, surfactant concentrations, aging times, etc., the emission spectrum in each batch of the core/shell formation is red shifted with respect to that of the core-only one (see Figure 2.8). The result reveals that further increase of the core/shell particle size is mainly attributed to the shell passivation. Further photophysical supports were rendered by the enhancement of the quantum efficiency on the core/shell structure in comparison to the core only particles synthesized via the same approach. The results clearly reveal the existence of improved passivation as well as the protective type structure generated on the resulted core/shell particles. The shell passivation was also confirmed by comparing the resulted particle sizes from TEM micrographs, in which within an identical aging time the average size calculated for core/shell particles is larger than that of the core only. Taking the thickness of ZnS monolayer to be 0.31 nm,[24] the number of ZnS monolayer (ML) overcoated on CdSe of batches 4 and 6 in Figure 2.8 was estimated to be 1.5 and 3.6 ML, respectively.

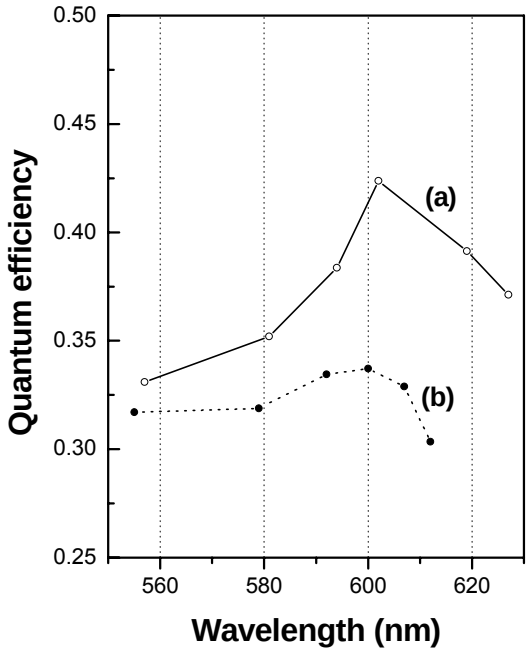

Figure 2.8 Control experiments performed on method 1 (tunable-size) with 6 different aging times (12 aliquots) are compared. Line (a) shows the evolution and properties of core/shell formation, while (b) depicts the properties of core only during the growth process. Note: the shell stock solution applied here for core/shell formation is zinc stearate/sulfur/TBP.

The above experiments/observations provide unambiguous evidence for the one-pot core/shell nanoparticles formation. One of our future aims is to develop chemically modified nanoparticles toward the biochemical application. To achieve this goal, we herein also demonstrated the feasibility of water-soluble quantum dots preparation based on the synthesized core/shell nanoparticles. In this preliminary study, a water-soluble 2-(12-Mecaptododecyloxy) methyl-15-crown ether capped CdSe@ZnS core/shell was prepared by a standard surfactant desorption/ligand exchange technique,[16,53] in which 2-(12-Mecaptododecyloxy) methyl-15-crown ether was synthesized by the alkylation of 2-(hydroxymethyl)-15-crown-5 ether with dibromododecane, followed by the replacement of the bromo- by thio- group in the presence of thiourea.[64,65] The resulted two different size QDs show naked eye detectable emission light with fluorescent quantum efficiency (Q.Y.) of 0.1, possessing about 30 nm bandwidth maximized at 580 nm and 636 nm, respectively (see Figure 2.9). In a comparative study, the same synthetic protocol was applied on the core-only CdSe. The fluorescence of the resulting water-soluble CdSe was completely quenched in aqueous solution, possibly due to the lack of shell protection.

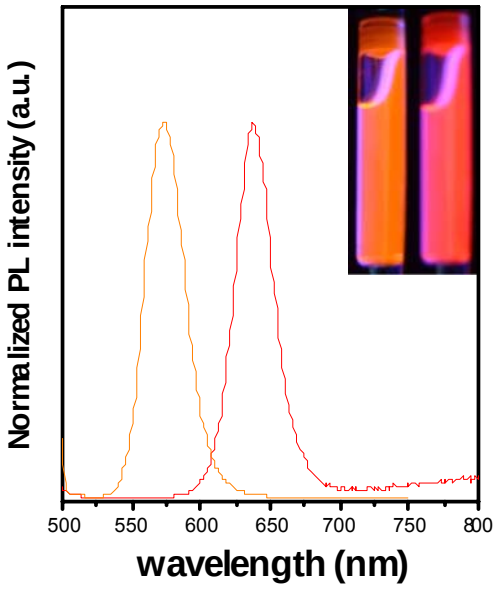

Figure 2.9 Emission spectra of two different size 2-(12-Mecaptododecyloxy) methyl-15-crown ether capped CdSe@ZnS nanoparticles in aqueous solution (pH ~9). Inset shows the authentic emission color of these two water-soluble CdSe@ZnS quantum dots acquired by a hand-held UV lamp with 366-nm excitation.

2.3.3. Comparing Current Methods

Finally, comparisons have been made here regarding other synthetic approaches. Using CdO as a precursor, the synthesis of core Cd chalcogenides has been reported by exploiting a combination of TDPA (tetradecylphosphonic acid) /TOPO/TOP (tri-*n*-octylphosphine) ligands.[35] From the economic viewpoint, HDA used in this study is much less expensive than TDPA. Although TDPA exhibits higher reactivity than HDA in complexing CdO, the aging time for the complex formation can still be fully accomplished within 1 hr using HDA. As shown in Figure 2.10, using CdO as a precursor, in combination with the HDA ligand, we have also successfully prepared high-quality core CdSe with a uniform size distribution.[66,67] Obviously, this advantage may play a key role for future scaled-up production. As described in an earlier section, Reiss et al.[27] have developed a method incorporating safer agents into the core/shell preparation, yet TDPA and a nontrivial, two-step synthetic process are involved. In addition, the shell materials (zinc stearate/Se@toluene) applied in Reiss et al.'s work were found inappropriate in our one-pot reaction scheme, although the actual mechanism remains unsolved at this stage. To make a successful one-pot reaction, shell composites were modified by substituting toluene to TBP. Furthermore, we also succeeded in synthesizing CdSe@ZnS nanocrystals simply by replacing Se with sulfur powder, indicating the versatility and simplicity of the one-pot reaction scheme.

Using $Cd(CH_3)_2$ as a precursor encapsulated by HDA ligand, Talapin et al.[33] reported on the preparation of CdSe@ZnS nanocrystals based on a two-step synthesis incorporating preparation and separation of core CdSe, followed by the second

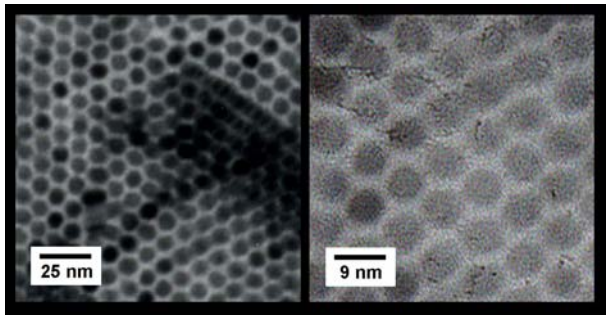

Figure 2.10 TEM image of core CdSe nanoparticles prepared from the CdO@HDA reaction system.

reaction involving pyrophoric Zn/S stock solution. Finally, via the $Cd(CH_3)_2$ precursor Hines and Guyot-Sionnest have reported on the one-pot synthesis of CdSe@ZnS nanocrystals in the TOP/TOPO system.[19] Under their reaction circumstance described, we have attempted to synthesize naocrystals via CdO precursors but unfortunately failed. Interestingly, in Hines et al.'s work, the spectral shift in terms of peak frequencies is small between core and core/shell, and could be explained by a decrease of the kinetic energy of the excited electron wavefunction upon spreading wavefunctions into the shell. In comparison, a wide range of tunability of 60 nm was consistently observed in our one-pot synthetic scheme. Similar phenomena were also observed in Talapin et al.'s work, indicating that the encapsulation of ZnS shell is accompanied by the growth of CdSe in HDA related systems.

2.3.4. *Preparation and Application of DHLA Capped CdSe@ZnS QDs*

The success in the preparation of DHLA capped CdSe@ZnS QDs was supported by the TEM image shown in Figure 2.11. In the case of QDs with 625-nm emission (5.3 ± 0.2 nm) a quantum yield of 0.18~0.25 in aqueous solution can be reproducibly prepared. As shown in Figure 2.12, except for the 625 nm emission attributed to the charge recombination, no additional band resulting from the deep trapped emission was observed in the region of 500-750 nm, demonstrating the superiority of core/shell QDs over the core-only QDs in view of the molecule/ion recognition. Figure 2.12 also shows the emission spectra of the QDs in neutral water titrated by $Hg(ClO_4)_{2(aq)}$ from 10^{-6} to 10^{-4} M. Apparently, the emission intensity decreased as the Hg^{2+} concentration ($[C_g]$) increased, while no

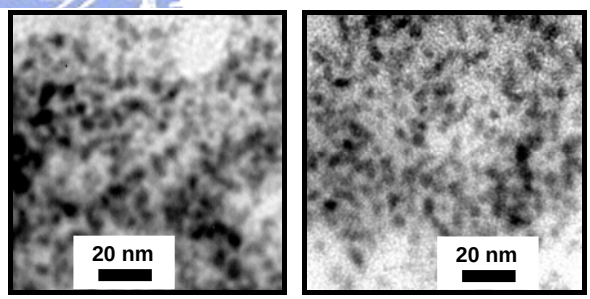

Figure 2.11 The TEM image of DHLA capped CdSe@ZnS nanoparticles before and after adding Hg^{2+} (1.6×10^{-4} M).

additional new band appeared throughout the titration. Taking the emission peak intensity of Hg^{2+}-free and Hg^{2+}-added QDs to be F_0 and F, respectively, the plot for $F_0/(F_0-F)$ versus $1/[C_g]$ revealed a straight line. (see **section 2.6.** Appendix for detailed derivation)

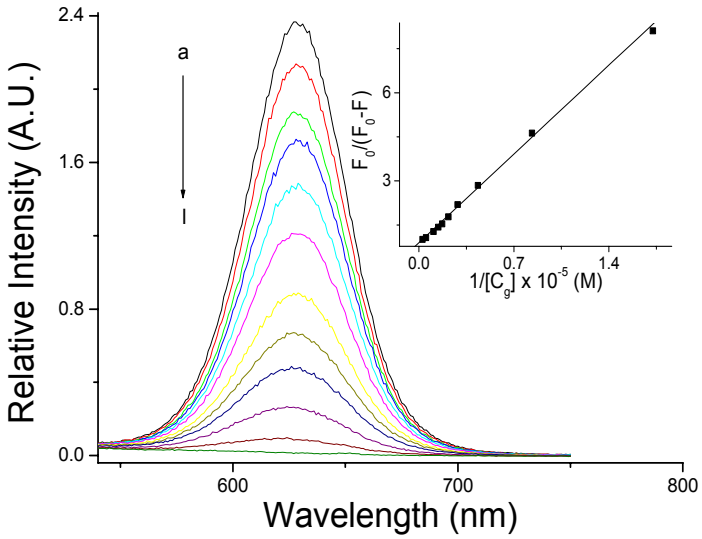

Figure 2.12 The fluorescence spectrum of CdSe@ZnS QDs (absorbance = 0.5 at 410 nm) in water (pH ~ 7) by adding $Hg(ClO_4)_2$ concentrations (C_q) of (a) 0, (b) 1, (c) 2, (d) 4, (e) 8, (f) 12, (g) 16, (h) 20, (i) 24, (j) 32, (k) 64, (l) 128 equiv (1 equiv = 1.2 x 10^{-6} M). Insert: The plot for $F_0/(F_0-F)$ versus $1/[C_g]$ (see text for definition). λ_{ex} : 410 nm.

The results indicate a 1:1 QDs:Hg^{2+} stoichiometry type of quenching process. Based on the slope and intercept of the plots, the equilibrium constant for the reaction/association of as high as $(2.5 \pm 0.2) \times 10^4$ M^{-1} was derived.

The titration experiments were also performed with the addition of other metal ions, including Pb^{2+}, Ba^{2+}, Zn^{2+} and Cd^{2+} specified by U. S. Environmental Protection Agency (EPA)[68] as common pollutants in drinking water as well as other metal ions such as Na^+, K^+, Ca^{2+}, Mn^{2+} and

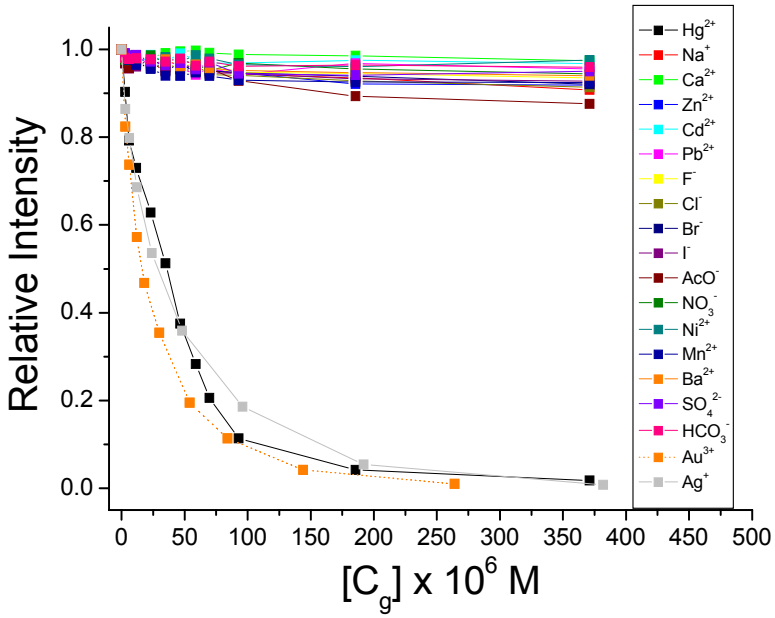

Figure 2.13 The plot of QDs fluorescence as a function of concentrations for various metal-ion salts and anions.

Ni^{2+} (in perchlorate salts). Regardless of their concentrations, negligible change in the emission intensity was observed upon increase of those metal ions up to 10^{-3} M. Similarly, the effect of anionic species was also examined by adding $NaNO_3$, NaOAc, $NaHCO_3$, Na_2SO_4 and various halogen anions (tetrabutylamonium salts) to the QDs/Hg^{2+} aqueous solution, and was found to cause negligible interference to the luminescence intensity (see Figure 2.13).

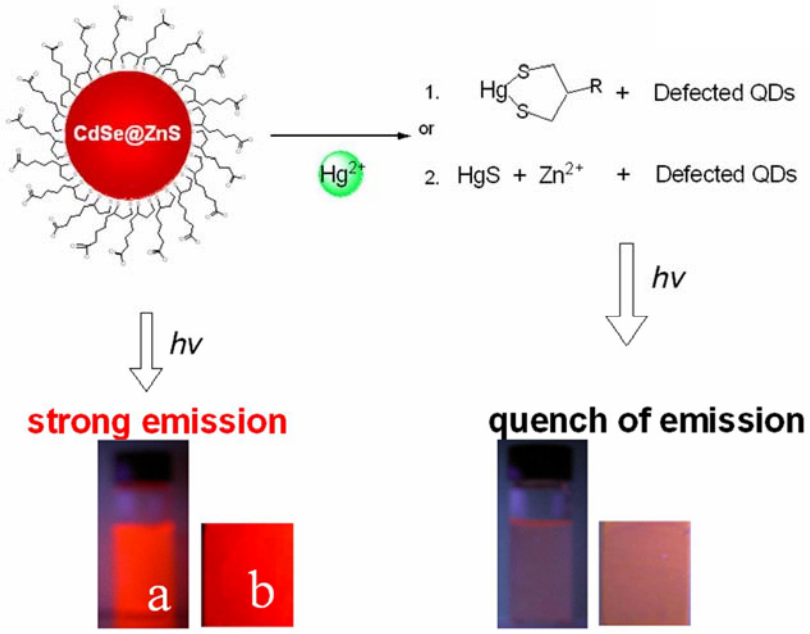

Figure 2.14 The tentatively proposed Hg^{2+} recognition mechanisms based on DHLA capped CdSe@ZnS QDs. The resulting fluorescence changes (a) in solution containing Hg^{2+} (1.6×10^{-4} M) and (b) in a TLC plate soaked in aqueous Hg^{2+} (5×10^{-5} M) solution for 20 seconds.

From the viewpoint of application, we have also examined whether a similar recognition capability can be applied in the heterogeneous solid film. To simplify the process, a silica-based TLC plate was used as a solid support. This was dipped into an aqueous solution containing QDs (optical density ~ 1.0 at 500 nm) for ~20 sec, and then vacuum-dried to remove water. With the use of a commercially available UV-lamp (366 nm) as an excitation source, bottom left of Figure 2.14 demonstrates the bright orange-red emission for the Hg^{2+}-free QDs soaked TLC plate, and, as shown in Figure 2.14b, drastic diminution of the emission was immediately observed

upon dipping the QDs coated TLC plate into an aqueous solution containing Hg^{2+} (5×10^{-5} M). In comparison, no change in either intensity or colour of the QDs emission upon being soaked in other metal-ions and anions applied above, regardless of their concentrations. The selectivity for Hg^{2+} can be shown by competitive experiments, in which the bright QDs emission in solution or TLC plate containing metal ions specified above (except for Hg^{2+}) immediately diminished upon being immersed in the Hg^{2+} solution (10^{-4}-10^{-6} M). Alternatively, the quenched emission in QDs/Hg^{2+} containing aqueous solution (or TLC plate) remained unchanged by the addition of metal ions specified above.

As supported by the lack of the growth of any new emission bands during Hg^{2+} titration, the quenching seems to be mainly due to the increase of the radiationless deactivation of QDs upon the addition of Hg^{2+}. This viewpoint can be further supported by the associated QDs decay dynamics shown in Figure 2.15. In the Hg^{2+}-free QDs solution, the 625-nm emission can qualitatively be fitted by single-exponential decay kinetics with a lifetime of ~30 ns. During the titration, we observed dual decay components. The slower one with the initial intensity decreased as increasing the Hg^{2+} concentration was fitted to be 20–30 ns, which, within experimental error, can be

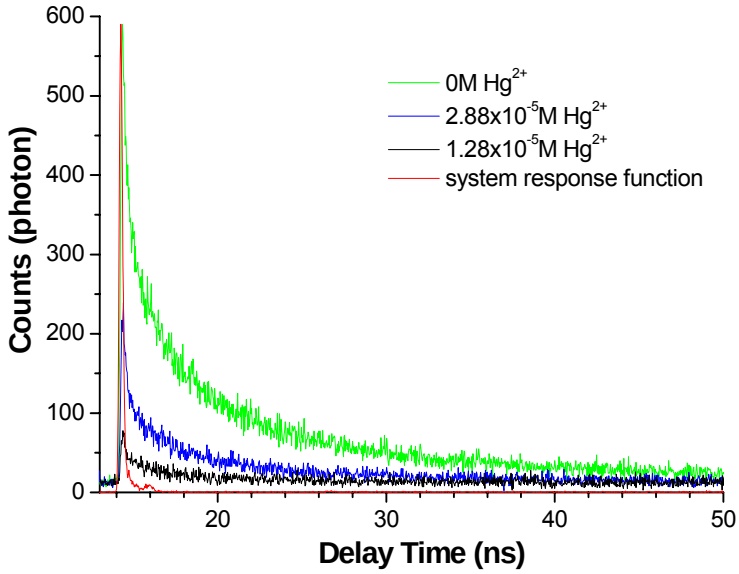

Figure 2.15 The decay dynamics of the QDs in H_2O at various added Hg^{2+} concentrations shown in the insert. Note that although the initial intensity of the long decay component decreases as increasing Hg^{2+}, its decay time constant more or less remains the same.

ascribed to the emission of the Hg^{2+}-free QDs. Conversely, the faster one was beyond the system response limit (~200 ps) and could reasonably be attributed to the Hg^{2+} reacted QDs. Since the titrant concentration was around 10^{-6}-10^{-4} M it is not likely that the system-response-limit nonradiative decay is induced by a bimolecular quenching process. Moreover, as indicated by the TEM image (Figure 2.11), both the shape and size of the QDs remained intact before and after adding Hg^{2+}. This, in combination with negligible changes of the absorption spectral features during the titration, rules out either the breakdown or self-assembly of the QDs during the Hg^{2+} titration.

Having gathered the above information, we herein tentatively propose two possible mechanisms, both of which incorporate the chemical reaction between Hg^{2+} and DHLA capped QDs. One proposed mechanism involves the redox reaction in that DHLA is oxidized to form a disulfide linkage and detached from QDs, accompanied by the reduction of Hg^{2+} that possibly co-deposits on the surface of QDs (see Figure 2.11). Alternatively, it would also be plausible that substituted reaction takes place between Hg^{2+} and the shell material ZnS, forming HgS on the QDs. Both reaction mechanisms create crystal defects, so that a deep trap of the electron may take place, resulting in drastic quenching of the emission intensity. For the latter case, a similar mechanism has recently been proposed by Liang et al.[69] based on the reaction of Ag^{+} with the mercaptoacetic acid capped, bovine serum albumin stabilized CdSe, forming Ag_2S on the surface. Both mechanisms would be able to make they possible to rationalize the high selectivity of Hg^{2+} mainly by the highest reduction potential for Hg^{2+} (0.851 eV)[70] among the studied metal ions catalogued by EPA as drinking water contaminants.[68] Another supportive evidence can be rendered by a titration pattern similar to that of Hg^{2+} for Ag^{+} (~0.80 eV) and Au^{3+} (1.50 eV, to Au^{0}),[70] the reduction

potentials of which are equivalent or higher than that of Hg^{2+} (see Figure 2.12 for the fluorescence titration). Note that Ag^{+} and Au^{3+} are not common pollutants catalogued in EPA.[68] However, since the actual surface nature of the QDs remains unclear, more advanced experiments are required to shed light on the actual reaction mechanism. For example, it has been previously proposed that Hg^{2+} could be used in the catalytic desulfurisation of organic moieties.[43] Thus, it is possible that a large portion of the dithiol linkages on the surface of QDs have been strip off due to a catalytic process. In this case, despite numerous dithiol capped sites provided for each QD to react with Hg^{2+}, a 1:1 (Hg^{2+}:QDs) reaction stoichiometry still holds, as determined from the fluorescence titration study.

2.3.5. *Preparation and Application of 15-Crown-5 Functionalized CdSe@ZnS Quantum Dots*

Figure 2.16A and B depict typical transmission IR spectra of neat MCE and MCE-capped CdSe@ZnS QDs, respectively. The gross resemblance in both spectral features and peak positions for several vibrational modes such as C-H stretching (2800-3000 cm^{-1}) and bending (~1100 cm^{-1}), and especially the C=O stretching motion of the ester functional group at 1732 cm^{-1} seems to guarantee a successful attachment of MCE onto CdSe@ZnS QDs. Further firm support of this viewpoint can be provided from the subtle differences between Figures 2.16A and B. As shown in the range of 2400-2600 cm^{-1}, the absence of S-H stretch band in Figure 2.16B unambiguously supports the formation of the CdSe@ZnS-sulfur bond. Figure 2.16C also depicts the TOPO capped CdSe@ZnS QDs prior to the modification with MCE. Apparently, the spectrum shown in Figure 2.16C is entirely different from that of Figure 2.16B. Especially, the characteristic band associated with TOPO at 1165 cm^{-1} (>P=O) disappears upon encapsulating MCE (see Figure 2.16B), suggesting that

MCE-capped particles have very few of adsorbed TOPO remained. In summary, various experimental evidences lead to a clear scheme that the preparation of MCE-capped CdSe@ZnS QDs was successful.

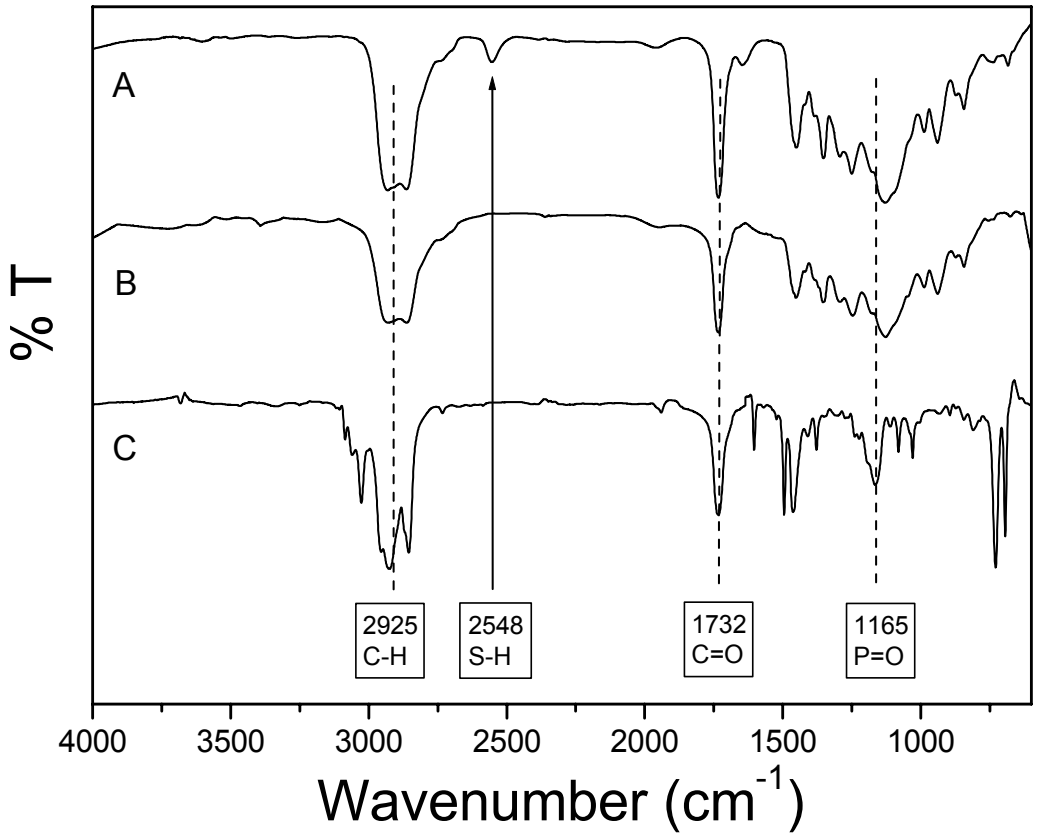

Figure 2.16 Transmission IR spectra of (A) neat MCE, (B) MCE-modified CdSe@ZnS QDs (5.6 nm/0.8 nm, KBr pellet), (C) TOPO capped CdSe@ZnS QDs. Note that the arrow pointing to the disappearance of S-H stretching in the MCE-modified CdSe@ZnS QDs.

Figure 2.17 depicted the fluorescence titration spectra of CdSe@ZnS (3.2/0.9 nm) and CdSe@ZnS (5.6/0.8 nm) QDs in water (pH ~ 7) by adding $KClO_4$ concentrations (C_g) up to ~ 1.8×10^{-3} M. To shorten the results and discussion, hereafter, the terms "green" (540 nm) and "red" (640 nm) QDs were used to represent CdSe@ZnS (3.2/0.9 nm) and CdSe@ZnS (5.6/0.8 nm), respectively, unless specified elsewhere. Also, for the clarity of the following discussion, the absorption spectrum of the corresponding QDs prior to the K^+ titration is also depicted. However, negligible changes on the absorption features were observed during the K^+ titration is also

depicted. Furthermore, it is difficult to determine the actual concentrations of green and red QDs due to the lack of precise molar absorptivity (extinction coefficient) for CdSe@ZnS QDs. Qualitatively, we simply took the ε value at 420 nm for green and red QDs to be the same as those for core only, i.e. CdSe (3.2 nm) $\varepsilon \sim 5.0 \times 10^4$ $M^{-1}cm^{-1}$ and CdSe (5.6 nm) $\varepsilon \sim 5.0 \times 10^5$ $M^{-1}cm^{-1}$, reported by Peng and coworkers.[71] Since green and red QDs were prepared to be 0.16 and 0.14 at 420 nm, the concentration was estimated to be 3.0×10^{-6} (green QDs) and 3.0×10^{-7} M (red QDs), respectively.

Prior to titration, dual emission was observed with peak wavelengths at 540 and 630 nm. Since the excitation spectra monitored at 540 and 630 nm resembled each individual, i.e. solely green or red QDs absorption spectra (not shown here), there is no interaction between the prepared green and red QDs. As a result, we can safely conclude that negligible energy or electron transfer takes place between green and red QDs in this dilute solution. Upon adding $KClO_4$, appreciable precipitation was promptly formed and visualized by naked eyes. This phenomenon can be best demonstrated by an experiment in that a single color CdSe@ZnS (4.8/0.8 nm) QDs was prepared and

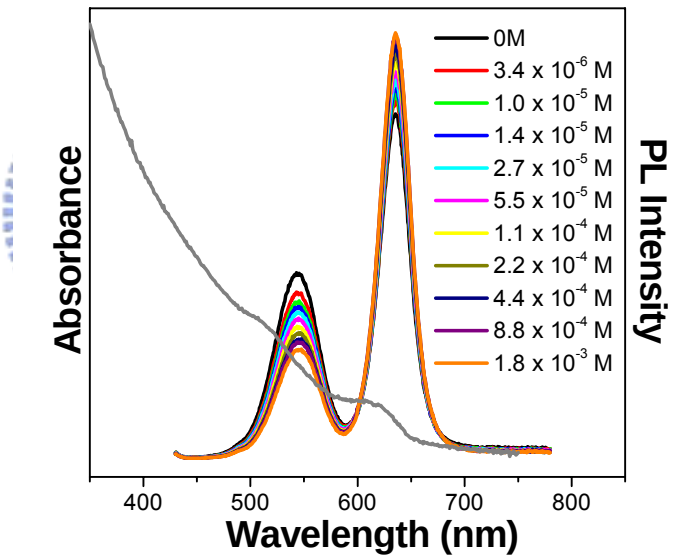

Figure 2.17 The fluorescence titration spectra of CdSe@ZnS (3.2/0.8 nm) and CdSe@ZnS (5.6/0.8 nm) QDs (absorbance = 0.15 at 420 nm) in water (pH ~ 7) by adding $Hg(ClO_4)_2$ concentrations (C_g) of (a) 0, (b) 1, (c) 2, (d) 4, (e) 8, (f) 12, (g) 16, (h) 20, (i) 24, (j) 32, (k) 64, (l) 128 (m) 256, (n) 512 equiv (1 equiv = 3.4×10^{-6} M). For the clarity of reading the absorption spectrum of the corresponding QDs prior to the K^+ titration is also depicted. However, negligible changes of absorption features were observed during the K^+ titration.

served as a host for the K^+ titration. As shown in Figure 2.18A-C, the K^+-free solution with bright orange-hue emission (λ_{max} ~ 595 nm) undergoes aggregation upon adding a batch of [K^+] of 2 × 10^{-2} M, resulting in a snowing-like luminescent QDs during the precipitation (λ_{ex} ~366 nm with a conventional UV lamp). Moreover, significant difference in the TEM images can be promptly perceived. For the case of K^+ free CdSe@ZnS (4.9/0.8 nm) the TEM images (see Figure 2.19) show semi-separately, dispersed particles, although the contrast for each individual QDs is vague possibly due to the interaction of MCE chains among QDs when concentrated. In contrast, an apparent aggregation of QDs was seen upon adding 10^{-2} M K^+. Because there are multiple binding sites (i.e. multivalency) on the sphere of MCE-capped QDs for the reversible complexation, the aggregates may be further evolved into a hexagonally close-packed structure. Unfortunately, the MCE interaction among QDs makes this evolution impossible.

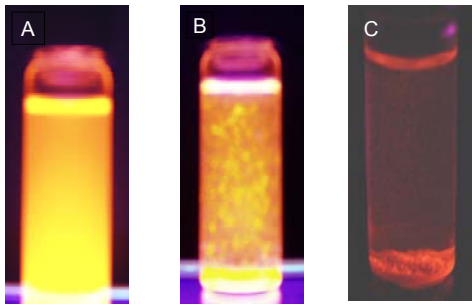

Figure 2.18 Photographs of (A) 54.9 nM CdSe@ZnS QDs in CH_3CN, and (B) subsequently addition of $KClO_4$ of 10^{-2}M. (C) Similar to (B) except for a span of 5 minutes.

It is well documented that the recognition of K^+ based on 15-crown-5 derivatives incorporates a 2**:**1 (15-crown-5: K^+) 15-crown-5/K/15-crown-5 sandwich type of association. Quantatively, Flink et al.[65] has determined the trimolecular formation constant of K^+ with 15-crown-5 in aqueous solutions to be as large as 27100 M^{-2}. In view of MCE-capped QDs, two possible binding schemes for

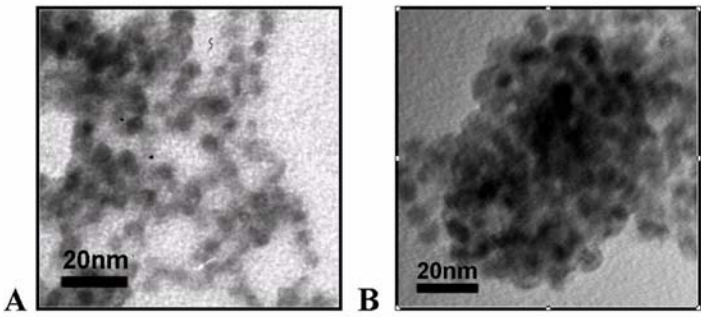

Figure 2.19 TEM micrographs of 15-crown-5 functionalized CdSe@ZnS (5.0/0.5 nm) QDs (A) before and (B) after addition of 0.1 mM K^+ into 54.9 nM colloidal CdSe@ZnS solutions.

the sandwich complexation are proposed, one of which incorporates two 15-crown-5 molecules from neighboring arms of the same QDs[64,65] clipping a K^+ ion (i.e. the intramolecular association). Alternatively, two 15-crown-5 molecules may originate from different QDs, forming an intermolecular type of association. For the intramolecular case, the exterior of sandwiched crown ethers and thus the entire nanoparticle may turn out to be hydrophobic. As a result, the polar aqueous medium enhances the van der Waal's interaction among hydrophobic nanoparticles, inducing the aggregation and subsequently the precipitation.[72] For the intermolecular type of recognition, QDs and K^+ are networked via sandwich complexes, followed by the precipitation as soon as the entire network becomes water insoluble (see Sceme 1).

Two key experimental results elaborated afterward support the mechanism of intermolecular association. First, Flink et al.[64] has determined that the Na^+ recognition by the 15-crown-5 molecules should be from 1:1 K^+/15-crown-5 association with a bimolecular association constant of 60 M^{-1} in aqueous solution. Thus, upon encapsulating Na^+ by 15-crown-5, the QDs become more hydrophobic, the structure of which should be very similar to intramolecular type of K^+ binding. However, given the fact that excess addition of Na^+ (~ 0.1 M) does not induce any precipitation, the scenario based on intramolecular type of association is less likely responsible for the efficient recognition of K^+.

Secondly, if the recognition mechanism were mainly based on the intramolecular association, there would be a lack of interplay between QDs. In contrast, for the case of dual color systems, the decrease (increase) of green (red) QDs intensity upon increasing the K^+ concentration strongly suggests the occurrence of energy transfer between green and red QDs bridged by K^+. Via semi-empirical (AM1) calculation, on the geometry optimized QD/K^+/QD, the distance between K^+ bridged two QDs was estimated to be ~30 Å. Thus, the occurrence of a Coulombic, i.e. Förster, type of

energy transfer is plausible. The rate of Förster type of energy transfer for an energy donor and acceptor separated by a distance r is given by

$$k_T(r) = \frac{Q_D k^2}{\tau_D r^6}\left(\frac{9000\ (\ln 10)}{128\pi^5 N n^4}\right)\int_0^\infty F_D(\lambda)\varepsilon_A(\lambda)\lambda^4 d\lambda \qquad (1)$$

where Q_D is the quantum yield of the donor in the absence of acceptor; n is the refractive index of the medium, which is typically assumed to be 1.4 for biomolecules in aqueous solution.; N is Avogadro's number; τ_D is the lifetime of the donor in the absence of acceptor; $F_D(\lambda)$ is the corrected fluorescence intensity of the donor in the wavelength range λ to $\lambda + \Delta\lambda$, with the total intensity (area under the curve) normalized to unity; $\varepsilon_A(\lambda)$ is the extinction coefficient of the acceptor at λ, which is typically in units of M^{-1} cm^{-1}; k^2 is a factor describing the relative orientation in space of the transition dipoles of the donor and acceptor and assumed to be equal to 2/3, which is appropriate for dynamic random averaging of the donor and acceptor. Note that in eq. 1 we wrote the transfer rate k_T as a function of r, and $k_T(\lambda)$, to emphasize its dependence on distance.

On the above basis, it is apparent that the 545 nm green emission overlaps well with the continuous absorption of red QDs. These, in combination with an ε value of ~ 5.4 × 10^4 $M^{-1}cm^{-1}$ around 545 nm for the red QDs and large transition dipole (short radiative lifetime of 50 ns, vide infra) for the green QDs, unambiguously support the occurrence of Förster, type of energy transfer upon K^+ association. Statistically, there will be three possible combinations regarding QDs/K^+/QDs association, namely the green/K^+/green, red/K^+/red and green/K^+/red structures, in which the probability of forming the green/K^+/red configuration is predicted to be 50% under the condition of equal molarity for green and red quantum dots. Supplementary support for the Förster type of energy transfer is provided by the decay dynamics. Figure 2.20 shows the relaxatgion dynamics of green QDs before and after the addition of K^+. In this

experiment the green QDs was monitored at 545 nm in a mixture of green and red QDs in CH_3CN free from K^+ (upper one). The decay can be well fitted by single exponential decay kinetics with an average lifetime of 18 ns. Similar to the upper trace, except for the addition of 10^{-3} M $KClO_4$, the decay trace is best fitted by two single exponential decay components with decay times of ~20 ns and 8.0 ns, indicating the occurrence of energy transfer and hence the reduction of green/K^+/red structure.

Finally, one remarkable feature is in that the luminescent properties are insensitive to addition of numerous physiologically important cations, such as Li^+, Cs^+, NH_4^+, Mg^{2+}, and Ca^{2+}. The high selectivity again indicates the formation of 2:1 sandwich complexes with K^+. The unusually large formation constants are attributed to the less polar environment inside the monolayers, which resembles the aforementioned less polar solvents.[64,65] Similarly, in this present study, the 15-crown-5 moiety poises at the interface of the aqueous phase and alkanethiol monolayers. The curvature of the nanoparticle renders a lower packing density further away from the surface and thus creates space facilitating preorganization of 15-crown-5 for K^+. Therefore, complexation of K^+ with MEC-capped QDs is facile in water.

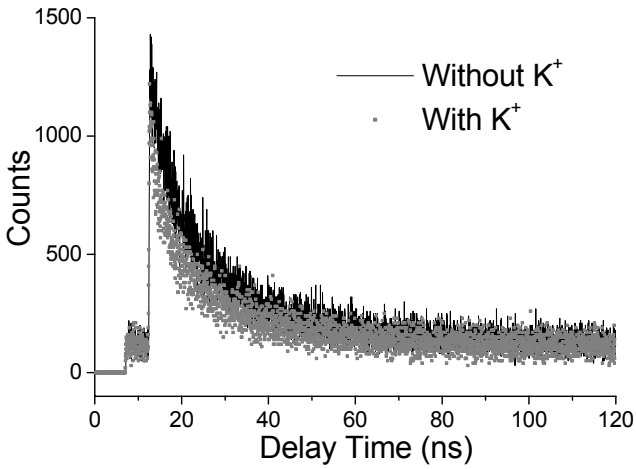

Figure 2.20 (black) The emission trace of green QDs monitored at 545 nm in a mixture of green and red QDs in H_2O. (gray) Similar condition, except for the addition of 1.8×10^{-3} M $KClO_4$, λ_{max} ~ 400 nm.

2.4. Conclusions

In the beginning of this chapter we have elaborated the strategy of one-pot syntheses of CdSe@ZnX QDs and it associated wavelength tunability and suitability. In view of convenience it is undoubted that one-pot reaction scheme can shorten the reaction time, whereas the fine-tuning of color is still feasible, if one does not greatly consider the quantum efficiency.

For the view point of applications, we have demonstrated a practical system based on DHLA capped CdSe@ZnS (core/shell) QDs to fluorogenically probe Hg^{2+} in aqueous solution and solid film at room temperature. Submicromolar sensitivity has been achieved promptly with this system, of which the mechanism is tentatively ascribed to crystal defects created by the substituted reaction between Hg^{2+} and DHLA capped QDs, resulting in the quench of the emission. The sensor is found to be highly selective, being insensitive to other metal ions of concern as drinking water pollutants. The high quantum yield, narrow-bandwidth and impurity-emission-free fluorescence make this DHLA capped CdSe@ZnS QDs suited to monitor Hg^{2+} environmentally.

In another approach, we have demonstrated that CdSe@ZnS QDs modified with 15-crown-5 in water exhibit excellent selectivity toward K^+. The recognition is achieved by aggregation networked by the QDs/K^+/QDs sandwich type of complexation depicted in Scheme 2.2. Single transduction can be achieved coarsely by precipitation and thus via the quenching of the fluorescence. Alternatively, in view of fine-tuning at low K^+ concentration, recognition can be reported through the sandwich type of association so that energy transfer takes place between dual color QDs. Unfortunately, due to the unknown multiple recognition sides for each QDs as well as the complicated network structure of the association, further quantitative studies such as the thermodynamics of complexation (association constant, free

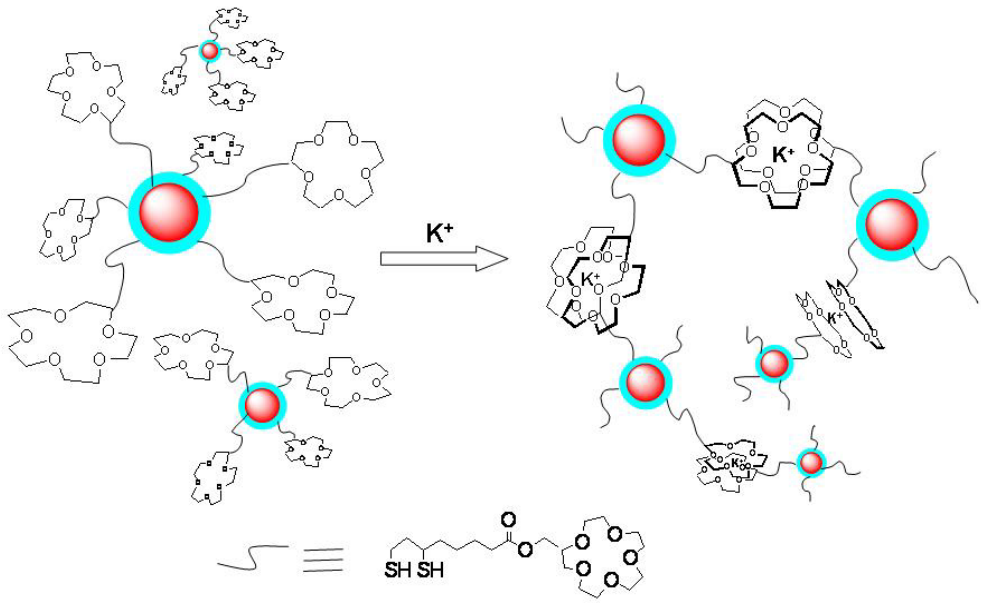

Scheme 2.2 The proposed K^+ recognition scheme through an intermolecular MCE-CdSe@ZnS| K^+| MCE-CdSe@ZnS sandwich type of association. Note that an intramolecular type of MCE-CdSe@ZnS| K^+| MCE-CdSe@ZnS association is quite unlikely due to a possible large steric barrier for the deformation of MCE.

energy, etc) cannot be resolved at this stage. Nevertheless, in a qualitative manner, other than extending the sensitivity range, we present the dual color energy transfer method as a general detection scheme, which renders a great versatility and flexibility in view of future applications.

2.5. References

1. Efros, Al. L.; Efros, A. L., *Sov. Phys. Phys. Semicond.*, **1982**, *16*, 772.

2. Brus, L. E., *J. Chem. Phys.*, **1984**, *80*, 4403.

3. Bawendi, M. G.; Steigerwald, M. L.; Brus, L. E., *Annu. Rev. Phys. Chem.*, **1990**, *41*, 477.

4. Brus, L. E., *Appl. Phys. A*, **1991**, *53* 465.

5. Wang, Y.; Herron, N., *J. Phys. Chem.*, **1991**, *95* 525.

6. Heath, J. R., *Science*, **1992**, *258* 1131.

7. Alivisatos, A. P., *Science*, **1996**, *271* 933.

8. Gaponenko, S. V., *Optical Properties of Semiconductor Quantum Dots*, Springer-Verlag, Berlin, **1996**.

9. Nirmal, M.; Brus, L. E., *Acc. Chem. Res.*, **1999**, *32* 407.

10. Efros, Al. L.; Rosen, M., *Annu. Rev. Mater. Sci.*, **2000**, *30* 475.

11. Jr. Bruchez, M.; Moronne, M.; Gin, P.; Weiss, S., A. P. Alivisatos, *Science*, **1998**, *281* 2013.

12. Chan, W. C. W.; Nie, S., *Science*, **1998**, *281* 2016.

13. Mattoussi, H.; Mauro, J. M.; Goldman, E. R.; Anderson, G. P.; Sundar, V. C.; Mikulec, F. V.; Bawendi, M. G., *J. Am. Chem. Soc.*, **2000**, *122* 12142.

14. Whaley, S. R.; English, D. S.; Hu, E. L.; Barbara, P. F.; Belcher, A. M., *Nature*, **2000**, *405* 665.

15. Niemeyer, C. M., *Angew. Chem.*, **2001**, *Int. Ed. 40*, 4128.

16. Rosenthal, S. J.; Tomlinson, I.; Adkins, E. M.; Schroeter, S.; Adams, S.; Swafford, L.; McBride, J.; Wang, Y.; DeFelice, L. J.; Blakely, R. D. *J. Am. Chem. Soc.* **2002**, *124*, 4586.

17. Chan, W. C.; Maxwell, D. J.; Gao, X.; Bailcy, R. E.; Han, M.; Nie, S., *Curr. Opin. Biotechnol.*, **2002**, *13*, 40.

18. Åkerman, M. E.; Chan, W. C. W.; Laakkonen, P.; Bhatia, S. N.; Ruoslahti, E., *PNAS*, **2002**, *99*, 12617.

19. Hines, M. A.; Guyot-Sionnest, P., *J. Phys. Chem.*, **1996**, *100*, 468.

20. Spanhel, L.; Haase, M.; Weller, H.; Henglein, A., *J. Am. Chem. Soc.*, **1987**, *109*, 5649.

21. Kortan, A. R.; Hull, R.; Opila, R. L.; Bawendi, M. G.; Steigerwald, M. L.; Carroll, P. J.; Bruset, L. E., *J. Am. Soc. Chem.*, **1990**, *112*, 1327.

22. Mews, A.; Eychmuller, A. V.; Giersig, M.; Schooss, D.; Weller, H., *J. Phys. Chem.*, **1994**, *98*, 934.

23. Danek, M.; Jensen, K. F.; Murray, C. B.; Bawendi, M. G., *Appl. Phys. Lett.*, **1994**, *65*, 2795.

24. Dabbousi, B. O.; Rodriguez-Viejo, J.; Mikulec, F. V.; Heine, J. R.; Mattoussi, H.; Ober, R.; Jensen, K. F.; Bawendi, M. G. *J. Phys. Chem. B* **1997**, *101*, 9463.

25. Gerion, D.; Pinaud, F.; Williams, S. C.; Parak, W. J.; Zanchet, D.; Weiss, S.; Alivisatos, A. P., *J. Phys. Chem.*, **2001**, *B 105*, 8861.

26. Malik, M. A.; O'Brien, P.; Re vaprasadu, N., *Chem. Mater.*, **2002**, *14*, 2004.

27. Reiss, P.; Bleuse, J.; Pron, A., *Nano lett.*, **2002**, *2*, 781.

28. Hoener, C. F.; Allen, K. A.; Bard, A. J.; Campion, A.; Fox, M. A.; Mallouk, T. E.; Webber, S. E.; White, J. M. *J. Phys. Chem.* **1992**, *96*, 3812.

29. Danek, M.; Jensen, K. F.; Murray, C. B.; Bawendi, M. G. *Chem. Mater.* **1996**, *8*, 173.

30. Talapin, D. V.; Rogach, A. L.; Kornowski, A.; Haase, M.; Weller, H. *Nano Lett.* **2001**, *1*, 207.

31. Murray, C. B.; Norris, D. J.; Bawendi, M. G., *J. Am. Chem. Soc.*, **1993**, *115*, 8706.

32. Murray, C. B.; Kagan, C. R.; Bawendi, M. G., *Annu. Rev. Mater. Sci.*, **2000**, *30*, 545.

33. Peng, X.; Manna, L.; Yang, W.; Wickham, J.; Scher, E.; Kadavanich, A.; Alivisatos, A. P. *Nature* **2000**, *404*, 59.

34. de Mollo Donegá, C.; Hickey, S. G.; Wuister, S. F.; Vanmaekelbergh, D.; Meijerink, A., *J. Phys. Chem. B*, **2003**, *107*, 489.

35. Peng, Z. A.; Peng, X., *J. Am. Chem. Soc.* **2001**, *123*, 183.

36. Qu, L.; Peng, X., *J. Am. Chem. Soc.* **2002**, *124*, 2049.

37. Braininaa, K.Z.; Stozhko, N.Y.; Shlygina, Z.V., *J. Anal. Chem.*, **2002**, *57*, 945.

38. Descalzo, A.B.; Martinez-Mañez, R.; Redeglia, R.; Rurack, K.; Sato, J., *J. Am. Chem. Soc.*, **2003**, *125*, 3418.

39. Yoon, J.; Ohler, N.E.; Vance, D.H.; Aumiller, W.D.; Czarnic, A.W., *Tetrahedron Lett.*, **1997**, *38*, 3845.

40. Wang, X.; Lee, C.; Soo-Hyoung, S.; Kris, J.; Kumar, J.; Samuelson, L., *Nano Lett.*, **2002**, *2*, 1273.

41. Shi, G.; Jiang, G., *Anal. Sci.*, **2002**, *18*, 1215.

42. Chae, M.-Y.; Czarnic, A.W., *J. Am. Chem. Soc.*, **1992**, *114*, 9704.

43. Palomares, E.; Vilar, R.; Durrant, J. R. *Chem. Commun.* **2004**, 362.

44. Brust, M.; Bethell, D.; Schiffrin, D. J.; Kiely, C. J. *Adv. Mater.* **1995**, *7*, 795-797.

45. Grabar, K. C.; Freeman, R. G.; Hommer, M. B.; Natan, M. J. *Anal. Chem,* **1995**, *67*, 735-743.

46. Mirkin, C. A.; Letsinger, R. L.; Mucic, R. C.; Storhoff, J. J. *Nature* **1996**, *382*, 607-609.

47. Elghanian, R.; Storhoff, J. J.; Mucic, R. C.; Letsinger, R. L.; Mirkin, C. A**.** *Science* **1997**, *277*, 1078-1081.

48. Link, S.; El-Sayed, M. A. *J. Phys. Chem. B* **1999**, *103*, 8410-8426.

49. Demers, L. M.; Mirkin, C. A.; Mucic, R. C.; Reynolds, R. A., III; Letsinger, R. L.; Elghanian, R.; Viswanadham, G. *Anal. Chem.* **2000**, *72*, 5535-5541.

50. Kim, Y.; Johnson, R. C.; Hupp, J. T. *Nano Lett.* **2001,** *1*, 165-167.

51. Kreibig, U.; Vollmer, M. *Optical Properties of Metal Clusters*; Springer: Berlin, 1995.

52. Storhoff, J. J.; Lazarides, A. A.; Mucic, R. C.; Mirkin, C. A.; Letsinger, R. L.; Schatz, G. C. *J. Am. Chem. Soc.* **2000**, *122*, 4640-4650.

53. Lin, S. Y.; Liu, S. W.; Lin, C. M.; Chen, C. H. *Anal. Chem.* **2002**, *74*, 330-335.

54. Donegá, C. de M.; Hickey, S. G.; Wuister, S. F.; Vanmaekelbergh, D.; Meijerink, A. *J. Phys. Chem. B* **2003**, *107*, 489.

55. Mattoussi, H.; Mauro, J. M.; Goldman, E. R.; Anderson, G. P.; Sundar, V. C.; Mikulec, F. V.; Bawendi, M. G. *J. Am. Chem. Soc.* **2000**, *122*, 12142.

56. Gunsalus, I. C.; Barton, L. S.; Gruber, W. *J. Am. Chem. Soc.* **1956**, *78*, 1763.

57. Drake, J. M.; Lesiecki, M. L.; Camaioni, D. M. *Chem. Phys. Lett.* **1985**, *113*, 530.

58. Yu, W.; Peng, X. *Angew. Chem., Int. Ed. Engl.* **2002**, *41*, 2368.

59. Donegá, C. de M.; Hickey, S. G.; Wuister, S. F.; Vanmaekelbergh, D.; Meijerink, A. *J. Phys. Chem. B* **2003**, *107*, 489.

60. Mekis, I.; Talapin, D. V.; Kornowski, A.; Haase, M.; Weller, H. *J. Phys. Chem. B* **2003**, *107*, 7454.

61. Peng, X.; Schlamp, M. C.; Kadavanich, A. V.; Alivisatos, A. P. *J. Am. Chem. Soc.* **1997**, *119*, 7019.

62. Wang, W.; Germanenko, I.; El-Shall, M. S. *Chem. Mater.* **2002**, *14*, 3028.

63. Zhou, S. M.; Feng, Y. S.; Zhang, L. D. *J. Crystal Growth* **2003**, *252*, 1.

64. Flink, S.; Boukamp, B. A.; van den Berg, A.; van Veggel, F. C. J. M.; Reinhoudt, D. N. *J. Am. Chem. Soc.* **1998**, *120*, 4652.

65. Flink, S.; van Veggel, F. C. J. M.; Reinhoudt, D. N. *J. Phys. Chem. B* **1999**, *103*, 6515.

66. Leitner, W. *Science* **1999**, *284*, 1780.

67. Peng, X. *Chem. Eur. J.* **2002**, *8*, 335.

68. *The drinking water contaminants can see:* http://www.epa.gov/ebtpages/watewaterpollutants.html

69. Liang, J. G.; Ai, X. P.; He, Z. K.; Pang, D. W. *Analyst* **2004**, *129*, 619.

70. Lide, D.R. *CRC Handbook of Chemistry and Physics*; 74th ed., CRC Press, Inc., Florida, MA, 1993, p. **8**-21, **8**-23.

71. Yu, W. W.; Qu, L.; Guo, W.; Peng, X. *Chem. Mater.* **2003**, *15*, 2854-2860

72. Chen, S. *Langmuir* **1999**, *15*, 7551-7557.

2.6. Appendix

Based on a 1:1 QDs@Hg^{2+} ratio of the reaction and the assumption of negligible consumption of the Hg^{2+}, the stoichiometry of the reaction can be expressed as

	QDs	+	Hg^{2+}	⇌	QDs (defected) + associated product
Initial	C_0		C_g		0	0
Final	C_0-C_p = C_M		C_g-C_p~ C_g		C_p	C_p

Prior to the addition of $Hg(ClO_4)_2$, the absorbance A_0 of QDs can be expressed as

$$A_0 = \varepsilon_M C_0 = -\frac{1}{2.303}\ln(1-\frac{I_{ab}}{I_0}) \sim \frac{I_{ab}}{2.303 I_0}$$
$$\therefore I_{ab} = 2.303 C_0 \varepsilon_M I_0$$

Where ε_M is the molar extinction coefficient of QDs, I_0 and I_{ab} denote number of photons being applied and absorbed at a specific wavelength of e.g. 500 nm. The fluorescence intensity, F_0, of QDs should be proportional to $I_{ab}\Phi_M$ where Φ_M denotes the fluorescence yield of QDs, and can thus be expressed by $F_0 = 2.303\,\alpha I_0 \varepsilon_M C_0 \Phi_M$ where α is an instrumental factor including sensitivity,

alignment, etc. of the detecting system. After adding Hg^{2+}, $I_{ab} = 2.303 I_0(\varepsilon_M C_M + \varepsilon_p C_p)$, and based on a similar derivation, the fluorescence intensity F can be expressed by $F = 2.303 k I_0(\varepsilon_M C_M \Phi_M + \varepsilon_p C_p \Phi_p)$ where ε_p and Φ_p denote the molar extinction coefficient and fluorescence quantum yield of the defected QDs, respectively. Φ_M and Φ_p are assumed to be constant throughout the titration. Note that the reaction equilibrium constant K_a of the reaction can be expressed as

$$K_a = \frac{C_p}{C_M C_g} = \frac{C_0 - C_M}{C_M C_g} \qquad \therefore C_M = \frac{C_0}{K_a C_g + 1}$$

Consequently, $F = 2.303 k I_0[\varepsilon_M(\frac{C_0}{K_a C_g + 1})\Phi_M + \varepsilon_p(C_0 - \frac{C_0}{K_a C_g + 1})\Phi_p]$

$$\frac{F_0}{F_0 - F} = \frac{C_0 \varepsilon_M \Phi_M}{C_0 \varepsilon_M \Phi_M - \left(\frac{C_0}{K_a C_g + 1}\right)\varepsilon_M \Phi_M - \left(C_0 - \frac{C_0}{K_a C_g + 1}\right)\varepsilon_p \Phi_p}$$

$$= \frac{(K_a C_g + 1)\Phi_M \varepsilon_M}{K_a C_g (\Phi_M \varepsilon_M - \varepsilon_p \Phi_p)} = \frac{\Phi_M \varepsilon_M}{(\Phi_M \varepsilon_M - \Phi_p \varepsilon_p)}\left(\frac{1}{K_a C_g} + 1\right) \qquad (\mathbf{1})$$

For the case that Φ_p is ~0 equation (**1**) can be simplified and rewritten as

$$\frac{F_0}{F_0 - F} \approx \left(\frac{1}{K_a C_g} + 1\right) \qquad (\mathbf{2})$$

The validity of this approach can be examined from a linear plot for $F_0/(F_0 - F)$ versus $[\text{guest}]^{-1}$. Accordingly, K_a can be deduced from the ratio of the intercept versus the slope. Using data shown in Figure 2.9 of the text linear plots of $F_0/(F_0 - F)$ versus $[Hg^{2+}]^{-1}$ are depicted in the insert, supporting the 1:1 complex formation. K_a was then deduced to be ~ $(2.5 \pm 0.2) \times 10^4$ M^{-1}.